Full Length Article

MRI-derived bound and pore water concentrations as predictors of fracture resistance

Mary Kate Manhard [a,b], Sasidhar Uppuganti [c,d,e], Mathilde Granke [c,d,e], Daniel F. Gochberg [b,f,g], Jeffry S. Nyman [a,b,c,d,e], Mark D. Does [a,b,f,h,*]

[a] Biomedical Engineering, Vanderbilt University, Nashville, TN, United States
[b] Vanderbilt University Institute of Imaging Science, Vanderbilt University, Nashville, TN, United States
[c] Department of Orthopaedic Surgery & Rehabilitation, Vanderbilt University, Nashville, TN, United States
[d] Tennessee Valley Healthcare System, Department of Veterans Affairs, Nashville, TN, United States
[e] Center for Bone Biology, Vanderbilt University Medical Center, Nashville, TN, United States
[f] Radiology & Radiological Sciences, Vanderbilt University, Nashville, TN, United States
[g] Department of Physics and Astronomy, Vanderbilt University, Nashville, TN, United States
[h] Electrical Engineering, Vanderbilt University, Nashville, TN, United States

ARTICLE INFO

ABSTRACT

Accurately predicting fracture risk in the clinic is challenging because the determinants are multi-factorial. A common approach to fracture risk assessment is to combine X-ray-based imaging methods such as dual-energy X-ray absorptiometry (DXA) with an online Fracture Risk Assessment Tool (FRAX) that includes additional risk factors such as age, family history, and prior fracture incidents. This approach still does not adequately diagnose many individuals at risk, especially those with certain diseases like type 2 diabetes. As such, this study investigated bound water and pore water concentrations (C_{bw} and C_{pw}) from ultra-short echo time (UTE) magnetic resonance imaging (MRI) as new predictors of fracture risk. Ex vivo cadaveric arms were imaged with UTE MRI as well as with DXA and high-resolution micro-computed tomography (μCT), and imaging measures were compared to both whole-bone structural and material properties as determined by three-point bending tests of the distal-third radius. While DXA-derived areal bone mineral density (aBMD) and μCT-derived volumetric BMD correlated well with structural strength, they moderately correlated with the estimate material strength with gender being a significant covariate for aBMD. MRI-derived measures of C_{bw} and C_{pw} had a similar predictive ability of material strength as aBMD but did so independently of gender. In addition, C_{bw} was the only imaging parameter to significantly correlate with toughness, the energy dissipated during fracture. Notably, the strength of the correlations with the material properties of bone tended to be higher when a larger endosteal region was used to determine C_{bw} and C_{pw}. These results indicate that MRI measures of C_{bw} and C_{pw} have the ability to probe bone material properties independent of bone structure or subject gender. In particular, toughness is a property of fracture resistance that is not explained by X-ray based methods. Thus, these MRI-derived measures of C_{bw} and C_{pw} in cortical bone have the potential to be useful in clinical populations for evaluating fracture risk, especially involving diseases that affect material properties of the bone beyond its strength.

1. Introduction

Current methods for predicting fracture risk are X-ray based, most commonly dual-energy X-ray absorptiometry (DXA). DXA provides an areal measure of bone mineral density (aBMD) and then based on reference population data, a T-score (number of standard deviations below normal aBMD) is determined [1]. However, the use of aBMD to diagnose osteoporosis (T-score < −2.5) has low sensitivity—many fractures occur in those with normal-to-osteopenic T-scores (between −2.5 and −1) [2]. Moreover, the increase in fracture risk with age is greater than predicted by the age-related loss in bone mass or aBMD [3]. Because DXA is a 2D imaging technique, it is not particularly sensitive to the contribution of bone structure and architecture to whole bone fracture resistance. Quantitative computed tomography (QCT) and more recently high-resolution peripheral-QCT (HR-pQCT) are 3D imaging techniques that can provide clinical measurements of volumetric BMD (vBMD) as well as structural and architectural parameters.

While there is evidence that these methods find differences between fracture cases and non-fracture cases [4–7], there is an overlap in the imaging measures between these cases, and they do not fully explain the increased fracture risk with age. In effect, structure and mineral density are not the sole determinants of fracture resistance [8].

Risk factors of fracture include age, prior fracture incidents, alcohol consumption, family history, and use of corticosteroids. These factors are often included as additional predictors to aBMD when using the Fracture Risk Assessment Tool (FRAX) to assess a patient's probability of suffering a fracture within 10 years. While a useful calculator, these additional risk factors still have low sensitivity and specificity [9], especially for people with type 2 diabetes [10]. Missing from DXA and FRAX is the contribution of the collagen phase of bone to fracture resistance. Recently, ultra-short echo time (UTE) magnetic resonance imaging (MRI) has been used to image cortical bone [11–13]. Unlike micro-MRI (μMRI) that provides images of trabecular architecture [14,15] (akin to HR-pQCT), UTE-MRI has the potential to probe the water bound to collagen in addition to pore water, a presumptive surrogate of cortical porosity.

The water bound to the mineralized collagen matrix, or bound water, has a short transverse relaxation time constant (T_2), ≈ 400 μs at 3 T (the magnetic field strength), while the water in the pore space of cortical bone has a longer T_2 (1 ms–1 s) [16]. In ^1H nuclear magnetic resonance (NMR) studies using machined samples of human cortical bone, these bound and pore water signal components have been shown to correlate with the material properties of the bone as determined by mechanical tests in bending [17]. Bound water concentration (C_{bw}) decreases with age—possibly due to loss of matrix and/or the accumulation of non-enzymatic collagen crosslinks [18]—and positively correlates with peak bending strength [17] and crack initiation toughness [19]. As an indirect measure of porosity of the cortical bone [19], pore water concentration (C_{pw}) negatively correlates with bending strength of human cortical bone.

Various UTE MRI methods have the potential to clinically investigate bound and pore water of cortical bone, such as using bi-component analysis of the signal decay with echo time to find T_2^* values and relative signal of bound and pore water [20] or using a dual echo method to find a porosity index [11]. While C_{bw} and C_{pw} as determined by non-clinical methods correlate with the material properties of cortical bone [17,21], clinically translatable imaging-derived C_{bw} and C_{pw} have not yet been tested as predictors of whole bone mechanical properties. In this study, we used previously described T_2-selective magnetization preparations, adiabatic inversion recovery (AIR) and double adiabatic full passage (DAFP), in combination with UTE MRI to selectively image C_{bw} and C_{pw} in cortical bone [12,22,23].

While X-ray-based approaches give reasonably good estimates of bone mass and bone structure, the primary determinants of strength, fracture resistance is due to more than whole bone strength alone. Toughness, or the capacity of bone to dissipate energy during failure, is known to decrease to a greater extent with advanced aging than material strength (independent of structure) [24]. This loss in toughness is perhaps one reason older subjects are more likely to break a bone regardless of their BMD measurement. This study aimed to determine whether MRI-derived measures of C_{bw} and C_{pw} of cadaveric specimens correlate with the material properties of human cortical bone (such as strength and toughness) as determined by three-point bending tests of the distal-third radius, as well as to compare MRI measures with X-ray based imaging measures, aBMD (DXA) and vBMD (by high-resolution μCT).

Part of the evaluation of how MRI measures correlate with whole bone mechanical properties is the evaluation of how best to extract quantitative information from 3D MRI C_{bw} and C_{pw} maps. Though several groups have quantified MRI-derived measures of bone, the best way to analyze and draw information from the maps remains unclear. A previous study found that small regions of interest (ROIs) inside the bone may miss changes in porosity relevant for predicting fracture [11]. In addition, when using an ROI that includes the whole bone, the determination of segmentation of cortical bone from surrounding tissue, particularly at the endosteal boundary, may significantly alter the information content of C_{bw} and C_{pw} measures. For example, the endosteal region has been shown to be the first to deteriorate when bone loss occurs [25–28], and therefore may be important for identification of increasing fracture risk. In this study, we investigate this problem by evaluating and comparing multiple methods of extracting quantitative information from MR images.

In summary, the purpose of this study was to evaluate the usefulness of whole bone imaging properties in predicting whole bone biomechanical properties. This was assessed with cadaveric radii by comparing material properties of the bone, as determined by three-point bend testing, to quantitative measures derived from MRI, DXA, and μCT images. Methods of deriving quantitative measures from MRI maps were also assessed.

2. Materials and methods

2.1. Cadaver specimen processing

The Vanderbilt Donor Program (Nashville, TN) supplied fresh human forearms (elbow to fingertip) from 40 cadavers (age 56 to 97, mean 80 ± 9.5, 20 male, 20 female). DXA and MRI measures were acquired on the whole intact arms (Fig. 1), and subsequently, the radii were dissected out and cut 7.5 cm proximally from the distal third of the bone using a circular low-speed, water irrigated, diamond-embedded band saw (South Bay Technology Inc., Model 660-1534). Following dissection, μCT imaging was performed on the radii with the bone immersed in a phosphate-buffered saline (PBS) medium at pH 7.4 during the scan. All imaging measurements were performed at the distal-third site of the radius. Lastly, the distal-third site was tested to failure in a three point bending (Fig. 2). The specimens were kept for a maximum of 48 h before being returned to the Vanderbilt Donor Program. When not being analyzed, the specimens were stored at 4 °C to prevent multiple freeze–thaw cycles.

2.2. MRI

The forearms were imaged with a Philips Achieva (Best, NL) 3 T scanner using the 8-channel knee coil for receive and the body coil for transmission. A short-T_2 reference phantom ($CuSO_4$-doped 10% H_2O:90%D_2O) in the field of view was used along with the signal equations to convert intensity into absolute units of concentration (mol ^1H/ L_{bone}) [29]. The AIR (for C_{bw} mapping) and DAFP (for C_{pw} mapping) sequences were used for acquiring C_{bw} and C_{pw} on each forearm using a 3D radial readout with uniform sampling on a sphere [30]. Images were reconstructed using either standard Philips base code or reconstructed off-line using measured gradient trajectories. (In general, the latter approach was needEd.) The k-space trajectories were measured using a modified Duyn's method [31] on the x, y, and z axis. These trajectories were interpolated to the 3D radial spokes acquired and used in a gridding reconstruction [32] off the scanner.

The AIR sequence used a repetition time (TR) = 400 ms, an inversion time (TI) = 80 ms, and an eighth ordered hyperbolic secant (HS8) pulse for inversion. The DAFP sequence used a TR = 300 ms, delay time (TD) = 5 ms, and two consecutive HS8 pulses. Samples were acquired with a receiver bandwidth of 322 kHz along 124,992 radial half-spokes in k-space to uniformly sample on a sphere and cover a 250 mm^3 FOV at a 1 mm isotropic nominal resolution, for a total scan time of 39 min for the AIR sequence and 54 min for the DAFP sequence. As described in Manhard et al. [23], for each magnetization preparation in both AIR and DAFP scans, 16 spokes were acquired (3.5 ms TR per spoke) using a variable flip angle scheme with an initial flip angle of 12.5° and an effective flip angle of 60°.

The receive-coil sensitivity (B_1^-) map was characterized by computing the ratio of two low resolution UTE images using the knee coil for receive on one scan and the body coil for receive on the other. This map
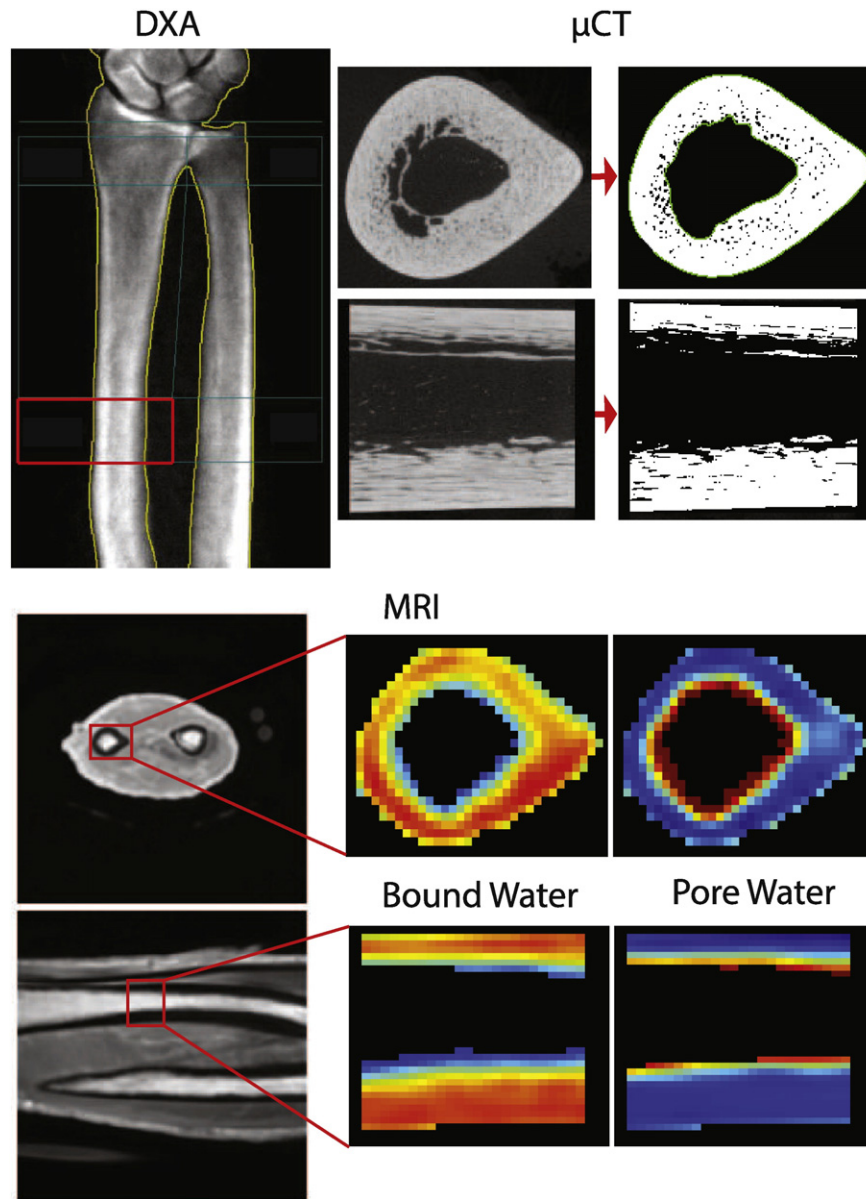
DXA

µCT

MRI

Bound Water   Pore Water

Fig. 1. The imaging modalities used on one representative radius, all analyzed at the same distal third section (shown in the red boxes). The top left shows the DXA scan, where the blue lines show how the aBMD is typically found in a clinical setting. The red box shows the distal-third section from which the aBMD was used in this study. The top right shows the µCT scan of the distal-third section of the radius in two planes with thresholded bone. The bottom images show a conventional UTE MRI scan in two planes with corresponding C_{pw} and C_{bw} maps.
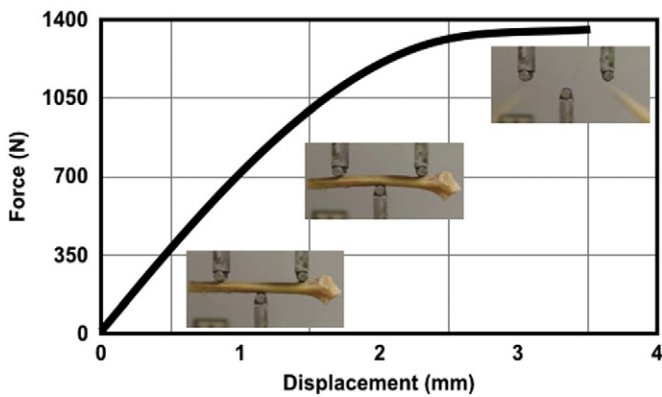

Fig. 2. Force displacement curve from a three point bend test of a representative radius. The test was performed at the distal third site, and images show the radius in multiple stages of breaking along the curve.

was smoothed with a 5×5 median filter to remove signal dropout in cortical bone regions and applied to the AIR and DAFP scans before quantitation.

Bone signal was quantified using signal equations [23] to solve for the relative spin densities of bound water, pore water, and the reference marker, and then converted to absolute units of concentration using the known concentration of the reference marker. A constant value of the longitudinal relaxation (T_1), transverse relaxation (T_2), and inversion efficiency (α) of bound water, pore water, and the reference marker was used across specimens. Bound water was estimated to have a $T_1/T_2/\alpha$ of 290 ms/350 µs/0.09, pore water was estimated to have a $T_1/T_2/\alpha$ of 450 ms/2600 µs/0.78, and the reference marker was estimated to have at $T_1/T_2/\alpha$ of 10 ms/10 ms/$-$0.83. Because the T_2 of the bone protons is on the order of the acquisition time, it is necessary to account for blurring of the signal that is induced by relaxation during the acquisition. As described in Manhard et al. [23], this signal loss or blurring factor (β) was estimated on a voxel-by-voxel basis using the known two-

dimensional geometry of the bone and an apodizing function that represents the blurring expected for a given location in k-space. The masked image of the bone is Fourier transformed into k-space, multiplied by the apodizing function to account for the effect of T_2^* blurring, and then inverse Fourier transformed back to image space to create a blurred mask.

The resulting C_{bw} and C_{pw} maps were analyzed by finding ROIs of the whole radius at the distal third section, through approximately 13 mm along the diaphysis of the bone. The ROIs were determined on a slice-by-slice basis using a polar segmentation method described by Rad et al. [29]. In brief, the bone marrow signal was first segmented using region growing [33], and the centroid of the bone marrow signal was found. A polar transformation was then performed about the centroid, and for each angle in the polar transformed image, the first and second peaks of the derivative of the 1D data were used to define the inner and outer boundary of bone. This mask was then transformed back into Cartesian image space. Because previous literature has shown a sensitivity to the information in the endosteal region related to fracture risk [28, 34], a second whole bone ROI was found by moving the inner boundary outward by a margin of 1.5 mm to decrease the amount of endosteal region that was classified as cortical bone. The outer periosteal boundary was left the same for both ROIs, as this boundary was better defined. The two ROIs for each bone were used to evaluate how the inclusion or exclusion of the endosteal region affected quantification of C_{bw} and C_{pw}, and, in-turn, the correlations between these measures and the strength and toughness measures. In each ROI, metrics computed for analysis included the mean, mode, median, maximum, minimum, first quartile (Q1), third quartile (Q3), and skewness of C_{bw} and C_{pw}. Correlations between each of these metrics for both ROIs were compared for significant differences.

2.3. Dual energy X-ray absorptiometry (DXA)

DXA scans of the forearm, while in a supine position on the bed, were acquired using a Lunar iDXA scanner (GE, Madison, WI) at the Vanderbilt Clinical Research Center (Fig. 1). From the scan, the areal bone mineral density (aBMD) was found in the standard area spanning 13 mm in the axial direction at the distal one-third site.

2.4. Micro-computed tomography (μCT)

The extracted radii were scanned using a Scanco μCT50 (Scanco Medical, Brüttisellen, Switzerland) at an isotropic voxel size of 48 μm (peak X-ray tube potential of 70 kVp, beam current of 200 μA, 1000 projections per 360°, 1500 ms integration time, beam hardening (BH) correction for 1200 mgHA/cm^3 material attenuation, 0.5 mm Al filter). The scan was centered at the distal third of the radius and included a stack of 13.056 mm (272 slices).

After reconstruction, the scans were analyzed by defining a contour around the endosteal and periosteal surfaces using the Scanco semi-automated contouring tool, which uses slice-by-slice hand contouring with snake algorithms to find edges and an interpolation function between slices [35]. The contoured images were segmented to separate bone material from background (Gaussian noise filter with a sigma of 0.2 and support of 2, lower threshold of 762.5 mgHA/cm^3). Apparent volumetric bone mineral density (vBMD) was the mean value of converted attenuation of all voxels within the contoured volume (mgHA/cm^3). Porosity was calculated by subtracting the bone volume over the total tissue volume from unity. Moment of inertia for the bending about minor axis (I_{min}), the distance between the centroid and the outer most layer for minor axis (c_{min}) and the mean total cross sectional area of the bone (Tt.Ar) were also determined using standard scripts provided by the manufacturer. Representative images from all imaging modalities used can be seen in Fig. 1.

2.5. Mechanical testing

The radii were subjected to a three point bending test (MTS 858 Bionix test system with a FlexTest SE controller) by loading the distal third radius, where the bone was imaged, at 6.5 mm/min until failure. Each hydrated bone was positioned with the anterior surface facing down and with the span supports adjusted to 80 mm (40 mm on either side of the distal-third site). The resulting force vs. displacement data (Fig. 2) was recorded at 100 Hz from a 14 kN load cell and the MTS linear variable displacement transducer (LVDT), respectively. Structural properties included the yield force (calculated at the point in which there was 15% loss in stiffness), the peak force, and work to fracture (area under the force vs. displacement curve). To calculate material properties, the flexure formula from beam theory (force × span × c_{min} / 4 / I_{min}) was used to determine both peak bending strength and yield strength. Modulus of toughness, or overall toughness, was the area under the stress vs. strain in which stress was determined by the aforementioned flexure formula and strain by 12 × displacement × c_{min} / span^2.

2.6. Statistical analysis

All statistical analysis was done with MATLAB (Mathworks, USA) and the MATLAB Statistics Toolbox. Since all imaging properties from the 40 radii were not normally distributed (as determined using a Kolmogorov–Smirnov test), Spearman's correlation coefficients (ρ) were used to evaluate the strength of the relationships between structural or material properties and imaging properties.

To determine to what extent gender explains the variance in each biomechanical property, potential predictors (age and imaging measures) were considered with gender as a categorical variable included in a general linear model. In addition, potential predictors that were not strongly inter-correlated ($\rho < 0.55$) were considered as independent predictors together in a general linear model to determine combinations of predictors that best explain the variance in the biomechanical properties. No more than two independent terms and the interaction between them were included in any given model. These linear models were then bootstrapped (1000 iterations) to account for the non-normality of the parameters. The predictors were considered significant if the p-value for the variable was less than 0.05.

3. Results

An overview of the two ROIs selected from MRI can be seen in Fig. 3. Mean signal-to-noise ratio (SNR) of the cortical bone signal in the MR images (defined as SNR = $\mu_S/(\mu_N/\sqrt{\pi/2})$, where μ_S is the mean signal in a region of cortical bone and μ_N is the mean signal in a region of background noise), was found to be 15 (range 5–45) for DAFP images and 12 (range 7–22) for AIR images. Slices from representative AIR and DAFP images of relatively strong and weak cadaveric arms are shown with the endosteal boundary lines overlaid and with the corresponding histograms of signal intensities resulting from each ROI used. The ROI that included more of the endosteal region (zone 1 + zone 2 in Fig. 3) gave a lower mean C_{bw} and a histogram that was skewed towards lower values compared to the ROI that excluded more of the endosteal region (zone 1 only in Fig. 3). The mean C_{pw} was higher for the larger ROI with a histogram skewed towards higher values. The change in histogram skewness between the two ROIs was more apparent in weaker bones.

Across all 40 bones, including more endosteal tissue resulted in an average 49% greater C_{pw} per voxel (range = 29–66%) and average 8% lower C_{bw} per voxel (range = −16–24%). These differences are not surprising—including more endosteal region will result in the inclusion of more signal from marrow—and highlight the sensitivity of these MRI measures to segmentation of cortical bone at the endosteal boundary.
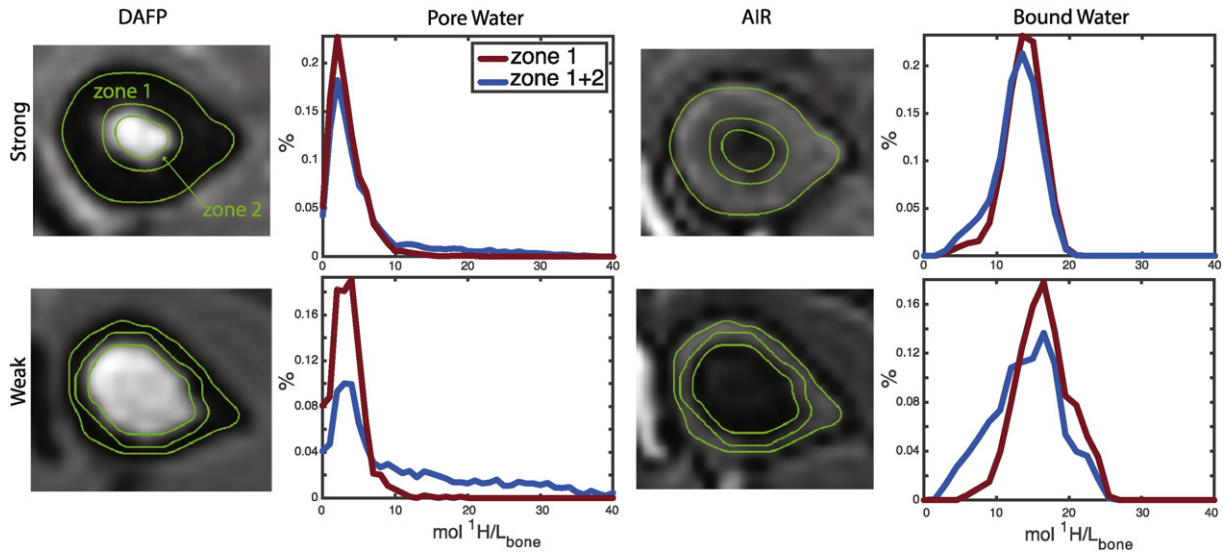
Fig. 3. DAFP and AIR images of a radius with high (top) and low (bottom) bending strength, with green lines showing boundaries for the different ROIs. The plots show histograms (in % of total) for the C_{bw} and C_{pw} found from the two ROIs. The blue shows histograms for the total bone area including the larger endosteal region (zone 1 + zone 2) and the red shows the smaller endosteal region only (zone 1).

Endosteal boundary definition will not only affect the magnitude of C_{bw} and C_{pw}, but also the relationship to mechanical properties of the whole bone. For example, Fig. 4 shows how correlations of bending strength with the mean and skewness of C_{bw} and C_{pw} are affected by the inclusion or exclusion of this endosteal region (zone 2).

Several metrics from the ROIs were correlated with biomechanical properties to evaluate the best way to extract quantitative information from the MRI-derived maps, including the mean, mode, median, maximum, minimum, Q1, Q3, and skewness. While all of the metrics of C_{pw} significantly correlated with strength and all the metrics of C_{bw} significantly correlated with both strength and toughness for both ROIs, there were no significant differences at the 95% confidence level between metrics or ROIs for either C_{bw} and C_{pw}. Table 1 gives an overview of correlations of the mean, median, and skewness for both ROIs with
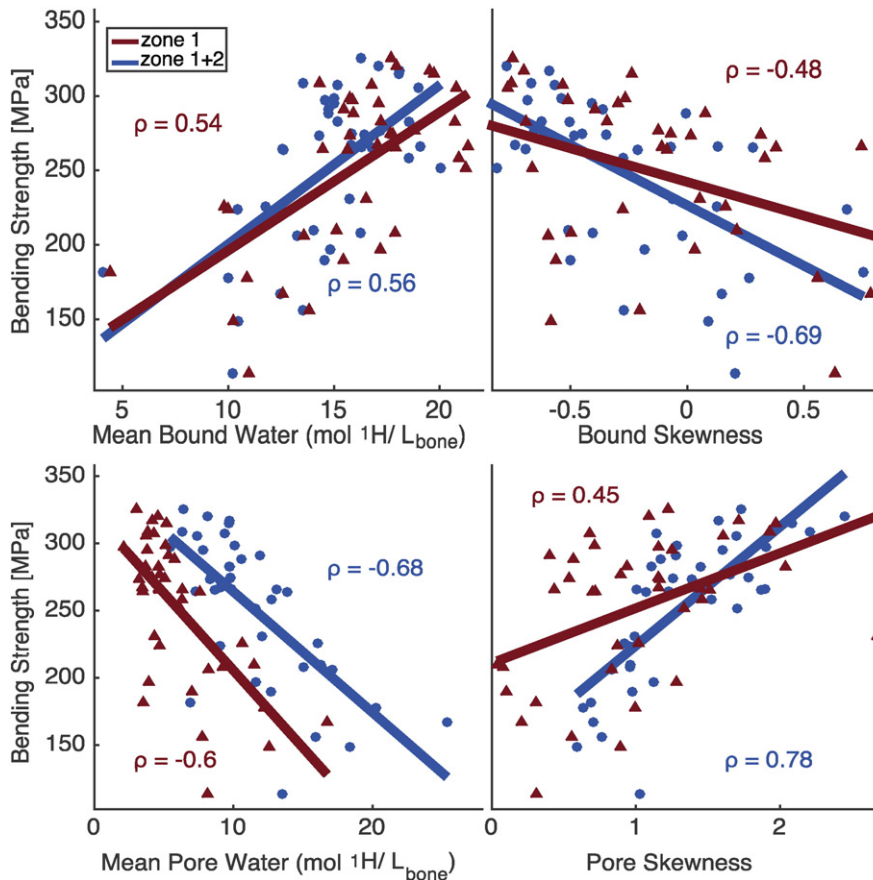

Fig. 4. Correlations of mean C_{bw} and C_{pw} (left) and skewness of C_{bw} and C_{pw} distributions (right) with bending strength. Blue lines show total bone area including the larger endosteal region and red lines shows the smaller endosteal region.

Table 1
Correlation coefficients between material properties and imaging properties for two regions of interest.

Spearman's ρ				
	Bound water	Mean	Median	Skewness
Bending strength	Zone 1 + zone 2	0.568	0.568	−0.687
	Zone 1	0.541	0.542	−0.478
Toughness	Zone 1 + zone 2	0.355	0.324	–
	Zone 1	0.342	–	–
	Pore water	Mean	Median	Skewness
Bending strength	Zone 1 + zone 2	−0.565	−0.744	0.783
	Zone 1	−0.597	−0.617	0.450

Spearman's correlation coefficient (ρ) for C_{bw} and C_{pw} metrics for two ROIs of the whole bone at the distal third site (zone 1 + zone 2—includes endosteal region, zone 1—does not include endosteal region) with material properties.

peak bending strength and toughness. Though not statistically different at the p < 0.05 significance level, correlation coefficients were higher in almost all cases when using the larger ROI that included more of the endosteal region (zone 1 + zone 2).

The skewness of both C_{bw} and C_{pw} also gave consistently higher correlations to strength when using the ROI that included the larger endosteal region. These higher correlations with skewness is not surprising because large pores, which tend to accumulate at the endosteal border [36], affect fracture resistance more than small pores [37,38], so even though there is not a substantial change in the mean, the skewness is sensitive to this change. Similarly, the median C_{pw} for the larger ROI gave higher correlations than the mean, which was expected since the distribution in the ROI is strongly skewed from normal. The mean and median C_{bw} performed similarly for both strength and toughness, as expected, since the distribution of C_{bw} was more normally distributed. To evaluate MRI C_{bw} and C_{pw} in comparison with DXA and μCT, the metrics with highest correlation coefficients were used—the skewness of C_{bw}

and C_{pw}, mean C_{bw}, and median C_{pw} from the ROI that included both zone 1 and zone 2.

An overview of the significance of potential predictors (age and imaging properties from all modalities) to structural properties of the radii (bending force and work to fracture) is shown in Table 2. These statistical analyses included gender as a covariate when significant. All imaging properties explained the variance in the structural properties, with the aBMD from DXA having the highest adjusted coefficient of determination (Adj-R$_2$) for peak bending force, and C_{bw} having the highest Adj-R$_2$ for work to fracture. Age had a lower explanation of the variance in structural strength (bending force) than any imaging property, and was not a significant explanatory variable for work-to-fracture. Yield strength predictions were similar to bending strength, and resulting correlations are shown in supplementary Table 1S and Fig. 1S.

Table 3 shows an overview of corresponding estimated material properties of the bone with statistical significance indicated for the same potential predictors. Gender was again used as a covariate in the general linear models when significant. While the predictive ability of all imaging parameters was lower for the estimated material strength than for structural strength of the radius, gender was no longer a significant covariate for any of the imaging properties except aBMD. In addition, the only imaging properties that significantly explained the variance in toughness were C_{bw} and porosity (which had a very weak correlation with toughness, though significant with gender as a significant covariate). Age again was the weakest predictor of strength compared to all imaging properties. Fig. 5 shows plots of correlations with fitted lines for these material properties and selected imaging properties.

Correlations between the non-destructive properties of the bone were also of interest to understand determinants of mechanical properties, and Fig. 6 shows median C_{pw} for each bone plotted against porosity from μCT, with the fitted regression line. In agreement

Table 2
Predictive ability of age and imaging measures with gender as a possible covariate for structural properties.

Structural property	Variable	Gender	Interaction	Linear model	Adj-R^2
Bending force	Age			M: 6120 − 51.9 ∗ Age	59.5
	p < .001	p = 0.004	p = 0.021	F: 1900 − 10.9 ∗ Age	
	aBMD			M: −161 + 2.76 ∗ aBMD	84.7
	p < .001	p < .001	n.s.	F: −705 + 2.76 ∗ aBMD	
	vBMD			M: −11,800 + 15.5 ∗ vBMD	64.3
	p < .001	p = 0.039	p = 0.021	F: −3400 + 4.89 ∗ vBMD	
	Porosity			M: 3430 − 128 ∗ Porosity	70.8
	p < .001	p < .001	p = 0.007	F: 1560 − 42.9 ∗ Porosity	
	C_{pw}			M: 3180 − 173 ∗ C_{pw}	72.8
	p < .001	p < .001	p = 0.004	F: 1590 − 59.1 ∗ C_{pw}	
	C_{pw}_Skew			M: −24.1 + 1410 ∗ C_{pw}_Skew	79.9
	p < .001	p = 0.380	p = 0.017	F: 171 + 713 ∗ C_{pw}_Skew	
	C_{bw}			M: −771 + 179 ∗ C_{bw}	68.5
	p < .001	p < .001	n.s.	F: −159 + 83.8 ∗ C_{bw}	
	C_{bw}_Skew			M: 1810 − 754 ∗ C_{bw}_Skew	60.5
	p < .001	p < .001	n.s.	F: 763 − 754 ∗ C_{bw}_Skew	
Work to fracture	Age			–	–
	n.s.	n.s.	n.s.		
	aBMD			M: 1210 + 4.8 ∗ aBMD	52.5
	p < .001	p = 0.004	n.s.	F: −235 + 4.8 ∗ aBMD	
	vBMD			M: −22,300 + 30.5 ∗ vBMD	41.8
	p = 0.009	p = 0.049	p = 0.034	F: 1860 + 0.97 ∗ vBMD	
	Porosity			M: 7790 − 254 ∗ Porosity	45.2
	p = 0.004	p < .001	p = 0.024	F: 2890 − 11.9 ∗ Porosity	
	C_{pw}			M: 7170 − 325 ∗ C_{pw}	40.3
	p = 0.035	p < .001	n.s.	F: 3340 − 60.7 ∗ C_{pw}	
	C_{pw}_Skew			M: 2740 + 1570 ∗ C_{pw}_Skew	45.5
	p = 0.004	p < .001	n.s.	F: 901 + 1570 ∗ C_{pw}_Skew	
	C_{bw}			M: −3160 + 521 ∗ C_{bw}	64.4
	p < .001	p = 0.027	p = 0.003	F: 1400 + 96.2 ∗ C_{bw}	
	C_{bw}_Skew			–	–
	n.s.	n.s.	n.s.		

M = Male, F = female, aBMD = DXA area bone mineral density, vBMD = μCT volumetric bone mineral density, C_{pw} = median pore water, C_{pw}_Skew = C_{pw} skewness, C_{bw} = mean C_{bw}, C_{bw}_Skew = C_{bw} skewness, n.s. = not significant.

Table 3
Predictive ability of age and imaging measures with gender as a possible covariate for structural properties.

Material property	Variable	Gender	Interaction	Linear model	Adj-R^2
Bending strength	Age			$451 - 2.49 * Age$	17.1
	p = 0.004	n.s.	n.s.		
	aBMD			M: $60 + 0.246 * aBMD$	63.8
	p < .001	p = 0.002	n.s.	F: $95 + 0.246 * aBMD$	
	vBMD			$-505 + 0.841 * vBMD$	37
	p < .001	n.s.	n.s.		
	Porosity			$336 - 7.1 * Porosity$	47.1
	p < .001	n.s.	n.s.		
	C_{pw}			$325 - 8.9 * C_{pw}$	53.3
	p < .001	n.s.	n.s.		
	C_{pw}_Skew			$136 + 88.4 * C_{pw}\_Skew$	55.2
	p < .001	n.s.	n.s.		
	C_{bw}			$93.6 + 10.7 * C_{bw}$	35.7
	p < .001	n.s.	n.s.		
	C_{bw}_Skew			$227 - 81.3 * C_{bw}\_Skew$	38.5
	p < .001	n.s.	n.s.		
Toughness	Age			–	–
	n.s.	n.s.	n.s.		
	aBMD			–	–
	n.s.	n.s.	n.s.		
	vBMD			–	–
	n.s.	n.s.	n.s.		
	Porosity			M: $9.63 - 0.205 * Porosity$	8.17
	p = 0.083	p = 0.020	p = 0.044	F: $5.17 + 0.102 * Porosity$	
	C_{pw}			–	–
	n.s.	n.s.	n.s.		
	C_{pw}_Skew			–	–
	n.s.	n.s.	n.s.		
	C_{bw}			M: $-0.267 + 0.488 * C_{bw}$	18.5
	p = 0.003	p = 0.040	p = 0.027	F: $6.41 + 0.00487 * C_{bw}$	
	C_{bw}_Skew			–	–
	n.s.	n.s.	n.s.		

M = Male, F = female, aBMD = DXA area bone mineral density, vBMD = μCT volumetric bone mineral density, C_{pw} = median pore water, C_{pw}_Skew = C_{pw} skewness, C_{bw} = mean C_{bw}, C_{bw}_Skew = C_{bw} skewness n.s. = not significant.

with previous studies [11,34,39], these parameters were highly correlated, giving us further confidence in the C_{pw} measurements as an indirect measure of porosity. There was also a moderate inverse correlation between C_{pw} and C_{bw} ($\rho = -0.48$, p = 0.002).

Results from multi-variable predictions of bending strength are shown in Table 4 for combinations of imaging parameters that gave better explanations of the variance than either parameter alone, regardless of whether gender was included as a significant covariate. One of the highest predictors of strength came from a combination of C_{bw} and C_{pw} or porosity. There were no significant multi-variable linear models for toughness.

4. Discussion

Fracture resistance depends not only on structural strength (load bearing capacity) but also on the ability of the tissue to dissipate energy (strain bearing capacity). Most prior cadaveric imaging studies reported significant correlations between structural properties and bone mineral density or bone structure and architecture, as determined by quantitative CT, DXA, or MRI [40–42], consistent with results found in this study. The present study also showed that measures of C_{bw} and C_{pw},

derived from UTE MRI correlated with the estimated material properties of bone. C_{bw} positively correlated with both strength and toughness, the latter of which did not correlate with μCT- or DXA-derived measurements. In addition, C_{bw} was not significantly correlated with μCT-derived tissue mineral density (TMD), and does not appear to be a surrogate for μCT- or DXA-derived measurements. Hydration of collagen is known to drastically affect brittleness of bone, although it remains to be determined what tissue characteristics influence C_{bw} [43]. C_{pw} negatively correlated with both yield and bending strength, and additionally was highly correlated with μCT porosity. While MRI-derived C_{pw} is sensitive to water in pores smaller than 48 μm (resolution of the μCT), the μCT measurements were collected at a higher resolution than is currently available clinically with HR-pQCT. The strong correlation between these two measures indicates C_{pw} gives an indirect measure of porosity. Unlike material strength correlations with DXA-derived aBMD, both C_{bw} and C_{pw} correlations were independent of gender. This difference may reflect the fact that aBMD depends on bone size, and thus gender [44]. The correlation between C_{bw} and C_{pw} was low enough that the two measurements could be used as independent variables together in a multivariate correlation, which resulted in a higher coefficient of correlation for bending strength than either alone.

This study found that MRI-derived imaging measures of whole bone significantly correlate with estimated material properties, consistent with previous studies using C_{bw} and C_{pw} measures from NMR of ex vivo bone samples [17–19]. Although three-point bending test of the whole bone yields an approximate measure of material properties, it uniquely allows for a direct comparison of the material properties with the whole-bone imaging measurements, all performed at the same anatomical location of the radius.

This study assessed the biomechanical properties of the distal-third radius, which is near a common site (wrist) of fragility fractures, easily imaged with 3D UTE MRI, and permits direct comparison to clinically relevant DXA measures. Though there are moderate correlations between radius strength and imaging properties acquired at different anatomical locations in the body (e.g., hip) [41], site-specific measurements have relatively high correlations with bone strength as determined by in vitro whole-bone testing [40,41]. Therefore, it would also be useful to evaluate these strength-imaging correlations in other common sites of fracture such as the lumbar vertebrae and the femoral neck. However, implementing UTE MRI methods in the lumbar vertebrae and femoral neck presents technical challenges due to the large FOV and high spatial resolution requirements, which would result in long scan times using the current 3D DAFP and AIR protocols. Alternate MRI protocols utilizing 2D acquisitions and/or reduced FOV would likely be necessary to assess such sites.

The MRI acquisitions in this ex vivo cadaveric study were performed with a relatively high resolution (1 mm) and large FOV (250 mm) to ensure coverage of the entire radius and to obtain maximal information about the bones from the images, which resulted in fairly high scan times. In practice, in vivo acquisitions can use a much smaller FOV for the wrist (~120 mm) and similar resolution (~1.2 mm) and still achieve reliable results [12] in clinically practical scan times. The scan times were reduced by acquiring 16 spokes per magnetization preparation, though this does increase the likelihood of bound water signal contaminating the signal for the DAFP sequence. With a shot-to-shot TR = 3.5 ms, approximately 10% of bound water signal will recover during acquisition, which could lead to pore water being overestimated by 1.8 (range 0.5–2.4) mol ^{1}H/L$_{bone}$ in bones with high bound water and low pore water.

Another potential source of error in the C_{bw} and C_{pw} maps is the inclusion of signal from bone marrow, particularly when using ROIs including the zone 2 region. While chemical shift artifacts for these scans is small (0.34 pixels) due to the high receiver bandwidth, including signal from bone marrow due to segmentation choices and partial volume averaging will likely lead to overestimation of pore water. While this is undoubtedly causing some overestimation in the pore
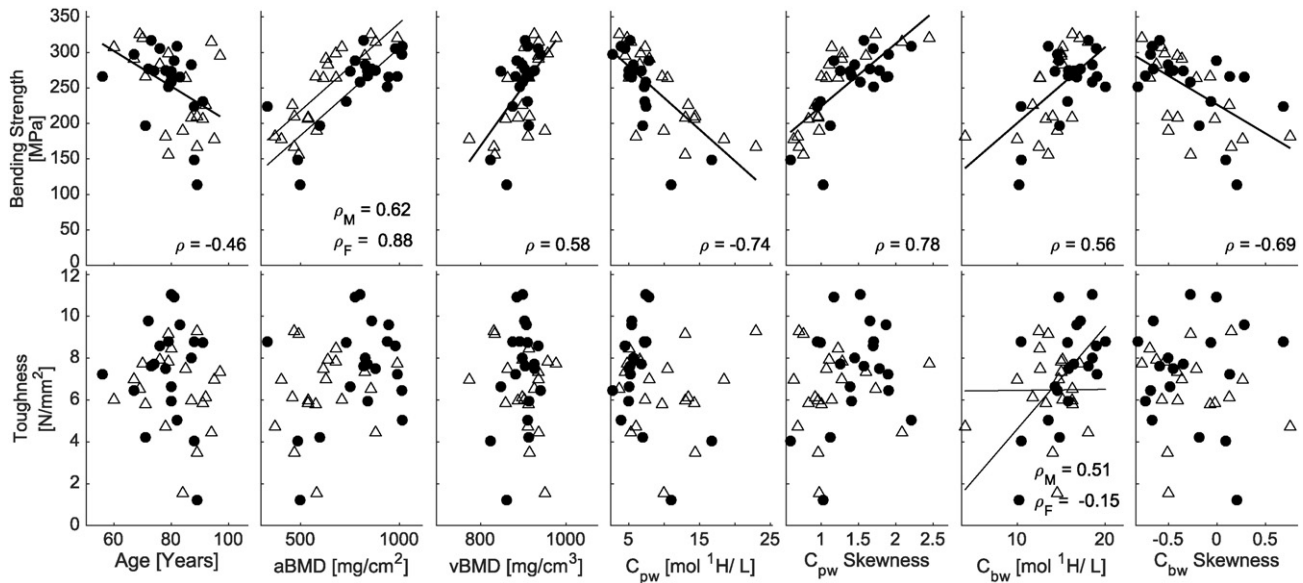
Fig. 5. Correlations of material properties (bending strength, and toughness) versus age and various imaging properties (aBMD from DXA, vBMD from μCT, and median C_{pw}, C_{pw} skewness, mean C_{bw}, and C_{bw} skewness from MRI) with corresponding Spearman correlation coefficient and p values. Open triangle—female, Solid circles—male.

water, the inclusion of the zone 2 area in the ROI still correlates well with biomechanical properties and in fact tends to give higher correlations than ROIs that exclude this area.

Though all of these sources of error of the MRI sequences used in this study have the potential to contaminate the resulting C_{bw} and C_{pw} measurements, C_{bw} and C_{pw} were still found to contain meaningful information about bone quality and fracture risk. In future studies, the MRI methods can be refined or other methods can be used to measure C_{bw} and C_{pw}, such as bi-component analysis, dual-band saturation, or dual-echo time porosity index. Improvements in methods will likely result in stronger correlations between the MRI-measures and bone material properties.

The importance of the ROI placement on assessing these MRI maps of bone is emphasized by the different C_{bw} and C_{pw} measures from the two ROIs with different endosteal boundaries (inclusion or exclusion of zone 2). Specifically, the same image has the potential to give different assessments of fracture risk depending on the extent to which the
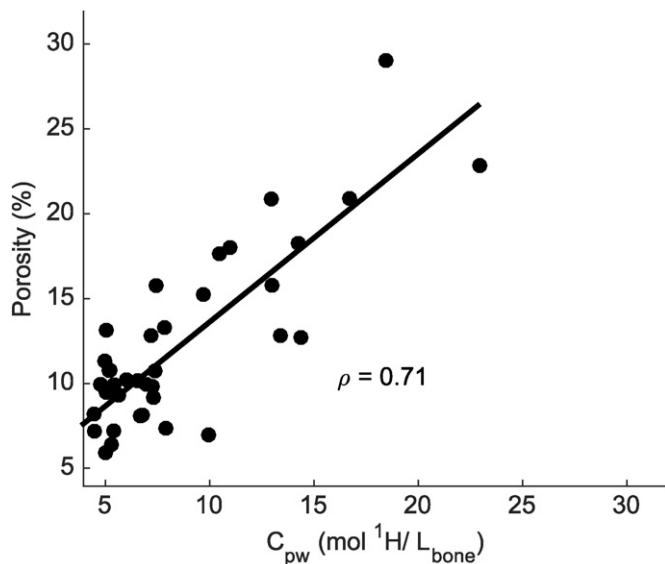
segmentation includes bone within the endosteal region where there can be a transitional zone in the elderly. While including or excluding the endosteal region may not severely affect correlations with strength and toughness, it is nevertheless important that segmentation is not user-dependent and is performed in a consistent and somewhat automated manner to get reliable results, since the C_{bw} and C_{pw} metrics themselves change significantly depending on the ROI. The effect of correlations also pertains when finding small regions inside of the bone instead of a whole bone segmentation. We tested this by finding several small ROIs inside the distal-third section of the radii, approximately ~4.5 mm^3 each. While mean C_{bw} and C_{pw} of these ROIs still correlated with strength and toughness, the correlations, though not significantly different, were consistently weaker than the whole bone correlations with strength and toughness.

It is also important to look beyond the mean water concentrations, especially given the skewness of the distribution of concentrations within a whole bone ROI. Bones with a high negative skewness of C_{pw} (shift towards lower concentrations) show higher strength, as well as bones with a high positive skewness of C_{bw} (shift towards higher concentrations). Though including more of the endosteal region risks

Fig. 6. Plot showing the correlation between C_{pw} from MRI and porosity from μCT with corresponding Spearman's correlation coefficient (ρ).

Table 4
Multivariate combinations of imaging measurements explaining the variance of material strength.

Variable 1[a]	Variable 2	Linear model[b]	Adj-R2
vBMD	C_{bw}	$0.424 * vBMD + 0.447 * C_{bw}$	52.2
p = 0.001	p < .001		
vBMD	C_{bw_Skew}	$0.402 * vBMD - 0.427 * C_{bw\_Skew}$	49.4
p = 0.003	p = 0.002		
vBMD	C_{pw_Skew}	$0.275 * vBMD + 0.589 * C_{pw\_Skew}$	59.2
p = 0.032	p < .001		
Porosity	C_{bw}	$-0.509 * Porosity + 0.39 * C_{bw}$	58.0
p < .001	p = 0.002		
Porosity	C_{bw_Skew}	$-0.504 * Porosity - 0.375 * C_{bw\_Skew}$	56.6
p < .001	p = 0.004		
C_{pw}	C_{bw}	$-0.566 * C_{pw} + 0.372 * C_{bw}$	63.5
p < .001	p = 0.002		
C_{pw}	C_{bw_Skew}	$-0.567 * C_{pw} - 0.373 * C_{bw\_Skew}$	63.6
p < .001	p = 0.001		

[a] vBMD = μCT volumetric bone mineral density, C_{pw} = median pore water, C_{pw_Skew} = C_{pw} skewness, C_{bw} = mean C_{bw}, C_{bw_Skew} = C_{bw} skewness.
[b] Standardized coefficients from the general linear model. No interactions were significant.

overestimating the mean C_{pw} or underestimating the mean C_{bw} by including voxels that may include marrow space, it is also capturing essential information that is sensitive to the degradation of bone. Dependable analyses of these maps are critical for future studies with C_{bw} and C_{pw} MRI.

Similarly, evaluating ROIs of μCT images for intra-cortical porosity is not straightforward. The current gold standard for evaluating quantitative μCT, as done in this study, involves semi-automatic hand contouring, which has some subjectivity. This is especially true near the endosteal boundary where the cortical bone transitions to trabecular bone. More automatic methods have been suggested for μCT evaluation [27,35], and may eventually be more useful in achieving efficient and repeatable results.

In conclusion, this study demonstrated that clinically relevant MRI images correlate with material properties of bone. C_{bw} and C_{pw} together could be used to help better predict fracture risk, especially in cases where DXA is currently inadequate. In particular, C_{bw} correlated with toughness while no other imaging properties were significantly correlated with this material property assessing the lack of brittleness. Future directions or applications include applying these C_{bw} and C_{pw} MRI methods in vivo to compare groups of patients at risk for fragility fracture. Finding differences between patients with fragility fractures and healthy subjects, as well as finding differences in C_{bw} and C_{pw} in response to various drug treatments, will help to further evaluate the significance of these quantitative MRI bone methods.

Acknowledgments

Appendix A. Supplementary data

Supplementary data to this article can be found online at http://dx.doi.org/10.1016/j.bone.2016.03.007.

References

[1] W.H. Organization, Technical Report: Assessment of Fracture Risk and Its Application to Screening for Postmenopausal Osteoporosis, 1994.
[2] T.M. Link, Osteoporosis imaging: state of the art and advanced imaging, Radiology 263 (2012) 3–17, http://dx.doi.org/10.1148/radiol.2633201203.
[3] J.A. Kanis, O. Johnell, A. Oden, A. Dawson, C. De Laet, B. Jonsson, Ten year probabilities of osteoporotic fractures according to BMD and diagnostic thresholds, Osteoporos. Int. 12 (2001) 989–995.
[4] C. Bergot, A. Laval-Jeantet, K. Hutchinson, I. Dautraix, F. Caulin, H. Genant, A comparison of spinal quantitative computed tomography with dual energy X-ray absorptiometry in European women with vertebral and nonvertebral fractures, Calcif. Tissue Int. 68 (2001) 74–82, http://dx.doi.org/10.1007/s002230001197.
[5] E.S. Orwoll, L.M. Marshall, C.M. Nielson, S.R. Cummings, J. Lapidus, J.A. Cauley, et al., Finite element analysis of the proximal femur and hip fracture risk in older men, J. Bone Miner. Res. 24 (2009) 475–483, http://dx.doi.org/10.1359/JBMR.081201.
[6] X.S. Liu, E.M. Stein, B. Zhou, C.A. Zhang, T.L. Nickolas, A. Cohen, et al., Individual trabecula segmentation (ITS)-based morphological analyses and microfinite element analysis of HR-pQCT images discriminate postmenopausal fragility fractures independent of DXA measurements, J. Bone Miner. Res. 27 (2012) 263–272, http://dx.doi.org/10.1002/jbmr.562.
[7] K.K. Nishiyama, H.M. Macdonald, D.A. Hanley, S.K. Boyd, Women with previous fragility fractures can be classified based on bone microarchitecture and finite element analysis measured with HR-pQCT, Osteoporos. Int. 24 (2013) 1733–1740, http://dx.doi.org/10.1007/s00198-012-2160-1.
[8] C.E.D.H. De Laet, B.A. van Hout, H. Burger, A. Hofman, H.A.P. Pols, Bone density and risk of hip fracture in men and women: cross sectional analysis, Br. Med. J. 315 (1997) 221–225.
[9] J.A. Kanis, D. Hans, C. Cooper, S. Baim, J.P. Bilezikian, N. Binkley, et al., Interpretation and use of FRAX in clinical practice, Osteoporos. Int. 22 (2011) 2395–2411, http://dx.doi.org/10.1007/s00198-011-1713-z.

[10] A.V. Schwartz, E. Vittinghoff, D.C. Bauer, T.A. Hillier, E.S. Strotmeyer, K.E. Ensrud, et al., Association of BMD and FRAX score with risk of fracture in older adults with type 2 diabetes, J. Am. Med. Assoc. 305 (2011) 2184–2192.
[11] C.S. Rajapakse, M. Bashoor-Zadeh, C. Li, W. Sun, A.C. Wright, F.W. Wehrli, Volumetric cortical bone porosity assessment with MR imaging : validation and clinical feasibility, Radiology 276 (2015) 526–535.
[12] M.K. Manhard, R.A. Horch, D.F. Gochberg, J.S. Nyman, M.D. Does, In vivo quantitative MR imaging of bound and pore water in cortical bone, Radiology 277 (2015) 221–229.
[13] M. Carl, G.M. Bydder, J. Du, UTE imaging with simultaneous water and fat signal suppression using a time-efficient multispoke inversion recovery pulse sequence, Magn. Reson. Med. 00 (2015) 1–6, http://dx.doi.org/10.1002/mrm.25823.
[14] R. Krug, S. Banerjee, E.T. Han, D.C. Newitt, T.M. Link, S. Majumdar, Feasibility of in vivo structural analysis of high-resolution magnetic resonance images of the proximal femur, Osteoporos. Int. 16 (2005) 1307–1314, http://dx.doi.org/10.1007/s00198-005-1907-3.
[15] G. Chang, C.M. Deniz, S. Honig, C.S. Rajapakse, K. Egol, R.R. Regatte, et al., Feasibility of three-dimensional MRI of proximal femur microarchitecture at 3 tesla using 26 receive elements without and with parallel imaging, J. Magn. Reson. Imaging 40 (2014) 229–238, http://dx.doi.org/10.1002/jmri.24345.
[16] R.A. Horch, J.S. Nyman, D.F. Gochberg, R.D. Dortch, M.D. Does, Characterization of 1H NMR signal in human cortical bone for magnetic resonance imaging, Magn. Reson. Med. 64 (2010) 680–687, http://dx.doi.org/10.1002/mrm.22459.
[17] R.A. Horch, D.F. Gochberg, J.S. Nyman, M.D. Does, Non-invasive predictors of human cortical bone mechanical properties: T(2)-discriminated H NMR compared with high resolution X-ray, PLoS ONE 6 (2011), e16359, http://dx.doi.org/10.1371/journal.pone.0016359.
[18] J.S. Nyman, Q. Ni, D.P. Nicolella, X. Wang, Measurements of mobile and bound water by nuclear magnetic resonance correlate with mechanical properties of bone, Bone 42 (2008) 193–199, http://dx.doi.org/10.1016/j.bone.2007.09.049.
[19] M. Granke, A.J. Makowski, S. Uppuganti, M.D. Does, J.S. Nyman, Identifying novel clinical surrogates to assess human bone fracture toughness, J. Bone Miner. Res. 30 (2015) 1290–1300, http://dx.doi.org/10.1002/jbmr.2452.
[20] J. Du, J.C. Hermida, E. Diaz, J. Corbeil, R. Znamirowski, D.D. D'Lima, et al., Assessment of cortical bone with clinical and ultrashort echo time sequences, Magn. Reson. Med. 70 (2013) 697–704, http://dx.doi.org/10.1002/mrm.24497.
[21] W.C. Bae, P.C. Chen, C.B. Chung, K. Masuda, D. D'Lima, J. Du, Quantitative ultrashort echo time (UTE) MRI of human cortical bone: correlation with porosity and biomechanical properties, J. Bone Miner. Res. 27 (2012) 848–857, http://dx.doi.org/10.1002/jbmr.1535.
[22] R.A. Horch, D.F. Gochberg, J.S. Nyman, M.D. Does, Clinically compatible MRI strategies for discriminating bound and pore water in cortical bone, Magn. Reson. Med. 68 (2012) 1774–1784, http://dx.doi.org/10.1002/mrm.24186.
[23] M.K. Manhard, R.A. Horch, K.D. Harkins, D.F. Gochberg, J.S. Nyman, M.D. Does, Validation of quantitative bound- and pore-water imaging in cortical bone, Magn. Reson. Med. 71 (2014) 2166–2171, http://dx.doi.org/10.1002/mrm.24870.
[24] X. Wang, X. Shen, X. Li, C.M. Agrawal, Age-related changes in the collagen network and toughness of bone, Bone 31 (2002) 1–7.
[25] N.M. Keshawarz, R.R. Recker, Expansion of the medullary cavity at the expense of cortex in postmenopausal osteoporosis, Metab. Bone Dis. Relat. Res. 5 (1984) 223–228.
[26] B. Clarke, Normal bone anatomy and physiology, Clin. J. Am. Soc. Nephrol. 3 (Suppl. 3) (2008) S131–S139, http://dx.doi.org/10.2215/CJN.04151206.
[27] R. Zebaze, A. Ghasem-Zadeh, A. Mbala, E. Seeman, A new method of segmentation of compact-appearing, transitional and trabecular compartments and quantification of cortical porosity from high resolution peripheral quantitative computed tomographic images, Bone 54 (2013) 8–20, http://dx.doi.org/10.1016/j.bone.2013.01.007.
[28] E. Perilli, Y. Bala, R. Zebaze, K.J. Reynolds, E. Seeman, Regional heterogeneity in the configuration of the intracortical canals of the femoral shaft, Calcif. Tissue Int. 97 (2015) 327–335, http://dx.doi.org/10.1007/s00223-015-0014-5.
[29] H.S. Rad, S.C.B. Lam, J.F. Magland, H. Ong, C. Li, H.K. Song, et al., Quantifying cortical bone water in vivo by three-dimensional ultra-short echo-time MRI, NMR Biomed. 24 (2011) 855–864, http://dx.doi.org/10.1002/nbm.1631.
[30] S.T.S. Wong, M.S. Roos, A strategy for sampling on a sphere applied to 3D selective RF pulse design, Magn. Reson. Med. 32 (1994) 778–784, http://dx.doi.org/10.1002/mrm.1910320614.
[31] P. Gurney, J. Pauly, D.G. Nishimura, A simple method for measuring B0 eddy currents, Proc. Int. Soc. Magn. Reson. Med. 13 (2005) 866.
[32] N.R. Zwart, K.O. Johnson, J.G. Pipe, Efficient sample density estimation by combining gridding and an optimized kernel, Magn. Reson. Med. 67 (2012) 701–710, http://dx.doi.org/10.1002/mrm.23041.
[33] R. Adams, L. Bischof, Seeded region growing, IEEE Trans. Pattern Anal. Mach. Intell. 16 (1994) 641–647.
[34] C. Li, A.C. Seifert, H.S. Rad, Y.A. Bhagat, C.S. Rajapakse, W. Sun, et al., Cortical bone water concentration : dependence of MR imaging measures on age and pore volume fraction, Radiology 272 (2014) 796–806.
[35] H.R. Buie, G.M. Campbell, R.J. Klinck, J.A. MacNeil, S.K. Boyd, Automatic segmentation of cortical and trabecular compartments based on a dual threshold technique for in vivo micro-CT bone analysis, Bone 41 (2007) 505–515, http://dx.doi.org/10.1016/j.bone.2007.07.007.
[36] C. Chappard, S. Bensalah, C. Olivier, P.J. Gouttenoire, A. Marchadier, C. Benhamou, et al., 3D characterization of pores in the cortical bone of human femur in the elderly at different locations as determined by synchrotron micro-computed tomography images, Osteoporos. Int. 24 (2013) 1023–1033, http://dx.doi.org/10.1007/s00198-012-2044-4.

[37] P. Broulik, J. Kragstrup, L. Mosekilde, F. Melsen, Osteon cross-sectional size in the iliac crest, Acta Pathol. Microbiol. Immunol. Scand. 90A (1982) 339–344, http://dx.doi.org/10.1111/j.1699-0463.1982.tb00104_90A.x.

[38] H. Brockstedt, M. Kassem, E. Eriksen, L. Mosekilde, F. Melsen, Age- and sex-related changes in iliac cortical bone mass and remodeling, Bone 14 (1993) 681–691.

[39] R. Biswas, W. Bae, E. Diaz, K. Masuda, C.B. Chung, G.M. Bydder, et al., Ultrashort echo time (UTE) imaging with bi-component analysis: bound and free water evaluation of bovine cortical bone subject to sequential drying, Bone 50 (2012) 749–755, http://dx.doi.org/10.1016/j.bone.2011.11.029.

[40] X.G. Cheng, G. Lowet, S. Boonen, P.H. Nicholson, G. Van der Perre, J. Dequeker, Prediction of vertebral and femoral strength in vitro by bone mineral density measured at different skeletal sites, J. Bone Miner. Res. 13 (1998) 1439–1443, http://dx.doi.org/10.1359/jbmr.1998.13.9.1439.

[41] E.-M. Lochmüller, C.A. Lill, V. Kuhn, E. Schneider, F. Eckstein, Radius bone strength in bending, compression, and falling and its correlation with clinical densitometry at multiple sites, J. Bone Miner. Res. 17 (2002) 1629–1638, http://dx.doi.org/10.1359/jbmr.2002.17.9.1629.

[42] T. Baum, M. Kutscher, D. Müller, C. Räth, F. Eckstein, E.-M. Lochmüller, et al., Cortical and trabecular bone structure analysis at the distal radius-prediction of biomechanical strength by DXA and MRI, J. Bone Miner. Metab. 31 (2013) 212–221, http://dx.doi.org/10.1007/s00774-012-0407-8.

[43] J.S. Nyman, L.E. Gorochow, R. Adam Horch, S. Uppuganti, A. Zein-Sabatto, M.K. Manhard, et al., Partial removal of pore and loosely bound water by low-energy drying decreases cortical bone toughness in young and old donors, J. Mech. Behav. Biomed. Mater. (2012), http://dx.doi.org/10.1016/j.jmbbm.2012.08.013.

[44] V. Naganathan, P. Sambrook, Gender differences in volumetric bone density: a study of opposite-sex twins, Osteoporos. Int. 14 (2003) 564–569, http://dx.doi.org/10.1007/s00198-003-1422-3.